Reduction of Artifacts in Multi-Energy Imaging for a Stationary Gantry CT Scanner

Seongjin Yoon, Alexander Katsevich, Michael Frenkel, Ed Morton, and William Thompson

***Abstract*—Multi-Energy Stationary Gantry CT (ME-SGCT) is a powerful tool for security screening. However, the SGCT geometry leads to an anisotropic voxel illumination pattern, which varies significantly across the field of view (FOV) and results in irregular-view streaks. Multi-Energy CT (MECT) exacerbates this artifact compared with single energy CT. In this paper, we use MECT reconstruction based on the Photoelectric (PE) and Compton Scattering (CS) decomposition. We propose two algorithms to address the ME-SGCT streaks: (1) modified bilateral filtering, which uses the more stable CS coefficient to filter the less stable PE coefficient, and (2) data-filling based on interpolation. We test the methods using simulated data for complex phantoms. The results demonstrate significantly reduced irregular-view streaks, which allows for more accurate estimation of the effective atomic number Z_{eff} and density ρ that are important for security screening.**

***Index Terms*—Multi-Energy CT imaging, Stationary Gantry CT, image reconstruction, modified bilateral filter, nonuniform view sampling, streak artifact reduction**

I. Introduction

At present, carry-on baggage screening is done on the basis of projection X-ray imaging, and the process relies heavily on the operator performance. In an effort to improve screening, there are several developments underway to use X-ray CT for these purposes. To meet the processing time requirement for the security check point, a stationary gantry CT (SGCT), which uses a distributed source and stationary detector, has been sought to provide the fastest possible scanning time.

While SGCT enables faster scanning, the design complicates the development of analytic reconstruction algorithms: (1) view-direction derivative cannot be used due to the X-ray source not following a well-defined trajectory, and (2) the illumination pattern of any voxel is highly anisotropic and varies significantly across the field of view. To address those issues, we previously developed a No View-Differentiation (NVD) type algorithm that incorporates a weight function. The latter is selected based on the illumination pattern to reduce streaks that arise due to irregular view sampling [1].

S. Yoon, A. Katsevich, and M. Frenkel are with iTomography Corp., Texas Medical Center Innovation Institute, 2450 Holcombe Blvd, Houston, TX 77021, USA (e-mail: syoon@iTomography.com, alexander@iTomography.com, michael@iTomography.com).

A. Katsevich is also with the University of Central Florida, Mathematics Department, Orlando, FL 32816, USA.

A. Katsevich is a shareholder and chief technology officer of iTomography Corporation and, as such, may benefit financially as a result of the outcomes of the work reported in this publication.

E. Morton and W. Thompson are with Rapiscan Systems, 2805 Columbia St, Torrance, CA 90503, USA (e-mail: emorton@rapiscansystems.com, wthompson@rapiscansystems.com).

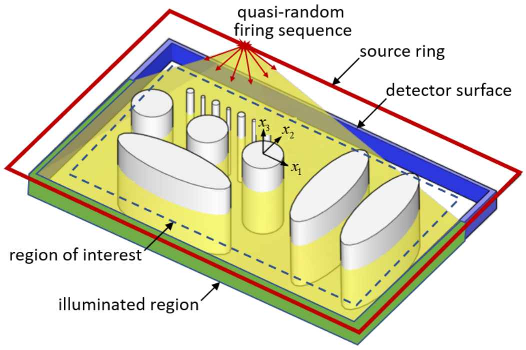

Fig. 1: Conceptual drawing of the SGCT scanner.

In an effort to improve threat detection even further, the SGCT system can incorporate a photon-counting detector with multiple energy bins to enable the scanner to capture spectral information. The Photoelectric (PE) and Compton Scattering (CS) decomposition method has been widely used as a foundation of multi-energy CT (MECT) reconstruction [2], [3]. In principle, PE-CS decomposition scheme can be directly used for MECT reconstruction from the spectral data collected by the SGCT scanner. However, the high dynamic range of the PE coefficient combined with inherent irregular-view streak artifacts of SGCT make it harder to use the reconstructed images for computing the physical properties of the scanned objects such as Z_{eff} and ρ. While the previously proposed weighted NVD reconstruction algorithm reduces irregular-view streak artifacts significantly, the PE-CS decomposition process can amplify the remaining streaks. The amplitude of the streaks in the PE coefficient can even exceed the amplitude of the original image, especially when metals are present in the field of view (FOV).

Here, we propose two methods to reduce the streak artifact in ME-SGCT: (1) modified bilateral filtering, which uses the more stable (smaller dynamic range) CS coefficient to filter the less stable (greater dynamic range) PE coefficient, and (2) data-filling based on interpolation. We test the proposed methods using simulated data. The tests show that the methods reduce the streaks significantly and enable one to more accurately estimate Z_{eff} and ρ pointwise in the FOV.

II. Basis Decomposition

Basis decomposition models for MECT have been widely used to simplify the reconstruction. The PE-CS decomposition was developed by Alvarez and Macovski [2] based on two major physical processes involved in photon attenuation at the range of medium energies (30-200 keV). The PE-CS model is given by the equation

$$\mu(E) = c_{\mathrm{p}} f_{\mathrm{PE}}(E) + c_{\mathrm{s}} f_{\mathrm{KN}}(E), \tag{1}$$

where E is the energy level, $f_{\mathrm{PE}} = 1/E^m$, f_{KN} is the Klein-Nishina function, and c_{p} and c_{s} are the PE and CS coefficients, respectively. The benefit of the PE-CS decomposition is that there exist semi-empirical formulas relating ρ, Z_{eff} with $c_{\mathrm{p}}, c_{\mathrm{s}}$:

$$c_{\mathrm{p}} = K_1 \frac{Z}{A} \rho Z^{n-1}, c_{\mathrm{s}} = K_2 \frac{Z}{A} \rho. \tag{2}$$

where K_1, K_2, and n need to be obtained empirically, assuming they are constant within the given energy range. The ratio Z/A is assumed to be 1/2. For this work, we use the parameters from Paziresh *et al.* [3]: $K_1 = 13.96$, $K_2 = 0.30$, and $n = 4.2$.

Since the noise in photon counting data is known to be Poisson distributed, we use Poisson likelihood to compute the estimates of C_{p} and C_{s}, which are the line integrals of c_{p} and c_{s}, respectively. The corresponding cost functional is given by:

$$\left[\widehat{C}_{\mathrm{p}}, \widehat{C}_{\mathrm{s}}\right] = \underset{C_{\mathrm{p}}, C_{\mathrm{s}}}{\arg\min} \sum_{l=1}^{N_l} h_l(\bar{y}_l(C_{\mathrm{p}}, C_{\mathrm{s}})), \tag{3}$$

where N_l is the number of detector energy bins. The Poisson likelihood function h_l and the estimated mean count $\bar{y}_l$ are defined as follows:

$$h_l(t) = t - y_l \log t, \tag{4}$$

$$\bar{y}_l(C_{\mathrm{p}}, C_{\mathrm{s}}) = \int_{E_l}^{E_{l+1}} I_l(E) \exp(-C_{\mathrm{p}} f_{\mathrm{PE}}(E) - C_{\mathrm{s}} f_{\mathrm{KN}}(E)) \mathrm{d}E, \tag{5}$$

where I_l is the energy spectrum within the l-th energy bin.

Once we get $\widehat{C}_p$ and $\widehat{C}_s$ from (3), we apply the view-density weighted NVD algorithm described in our previous work [1], to separately reconstruct c_p and c_s.

III. Image Domain Sparse-View/Noise Streak Reduction Filtering

Due to irregular view sampling, sparse-view streaks in ME-SGCT reconstructions are distributed irregularly across the FOV. Any conventional filter with localized support cannot effectively deal with such high amplitude irregularly distributed artifacts. To suppress the artifact while keeping the algorithm numerically simple and efficient, we introduce a *modified bilateral (MBL) filter guided by a reference image*:

$$\mathrm{MBL}[f(i)] = \sum_{j \in \Omega_{(i, n_{\mathrm{B}})}} \exp\left(\frac{-(g(i) - g(j))^2}{\sigma \max(\mathbf{g})^2 + \delta}\right) f(j), \tag{6}$$

where f is the image being filtered, $\Omega_{(i,n_{\mathrm{B}})}$ is the set of neighboring pixels in the square region centered at the i-th pixel with size $(2n_{\mathrm{B}} + 1) \times (2n_{\mathrm{B}} + 1)$, and σ and δ are tunable parameters. The latter also prevents dividing by zero. The spatial weight of the filter is constant within the square region. The Gaussian kernel is normalized by the maximum value of the reference image for the following two reasons: (1) to account for the dynamic range difference between c_{p} and c_{s}, (2) the most significant sparse-view streak component is proportional to the maximum value of each image. g is the reference image which contains information about the same object, but has a smaller dynamic range and less sparse-view streaks. This approach belongs in a group of multi-channel image denosing, see e.g. [4] and references therein.

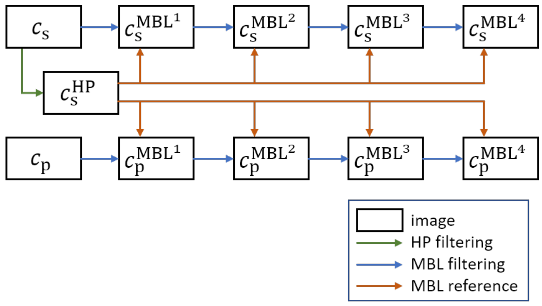

Fig. 2: Illustration of the image filtering workflow.

To obtain the reference image g, we first filter the reconstructed CS image c_{s} using edge-preserving hyperbolic potential (HP) regularization: $c_{\mathrm{s}} \to c_{\mathrm{s}}^{\mathrm{HP}}$. Since streak intensity is much lower in c_{s} than in c_{p}, the localized HP filtering can produce a good quality image $c_{\mathrm{s}}^{\mathrm{HP}}$ with most of the streaks removed. Instead of using $c_{\mathrm{s}}^{\mathrm{HP}}$ directly for subsequent processing, we use $g = c_{\mathrm{s}}^{\mathrm{HP}}$ as a reference image for MBL filtering of c_{s} to produce a new image $c_{\mathrm{s}}^{\mathrm{MBL}}$, then we apply the MBL filter to c_{p} using the same $c_{\mathrm{s}}^{\mathrm{HP}}$ as the reference image.

For both c_{p} and c_{s}, we apply the MBL filter four times with $c_{\mathrm{s}}^{\mathrm{HP}}$ as the reference image. See Fig. 2 for the diagram that illustrates the proposed image filtering workflow. Here, f^{MBL^n} represents the image f filtered by MBL n times. The reason why we use $c_{\mathrm{s}}^{\mathrm{HP}}$ for MBL filtering of c_{p} (even though $c_{\mathrm{s}}^{\mathrm{MBL}^4}$ is more accurate) is to have the same amount of blurring in $c_{\mathrm{s}}^{\mathrm{MBL}^4}$ and $c_{\mathrm{p}}^{\mathrm{MBL}^4}$. This leads to more accurate pointwise ratios $c_{\mathrm{p}}/c_{\mathrm{s}} \approx c_{\mathrm{p}}^{\mathrm{MBL}^4}/c_{\mathrm{s}}^{\mathrm{MBL}^4}$ when computing Z_{eff}.

While the MBL filter effectively removes high amplitude streaks, it comes with one caveat. For accurate reconstruction of a region with constant Z_{eff} and density, the size of the region should be large enough to contain sufficiently many streaks. In this case the streaks are reduced due to averaging. For voxels farther away from a high-Z material that generates streaks, it gets harder to remove sparse-view streaks because the frequency of the streaks is decreasing. To address this issue, we fill in some of the missing data by interpolating available data. This procedure is explained in the next section.

IV. Data Filling Using Interpolation

Adding to the MBL filtering described in Sec. III, we create synthetic data by interpolating two projection data with the same source-detector position (but the object is shifted) during the back-projection stage to reduce the streak artifact further.

Due to the rectangular geometry of the detector, we first project the data onto a virtual flat detector to use the conventional FDK-type backprojection. This backprojection process combines the horizontal axis (along the detector rows) of the virtual detector and the vertical axis (along the columns) of the actual detector to parametrize the data to be backprojected.

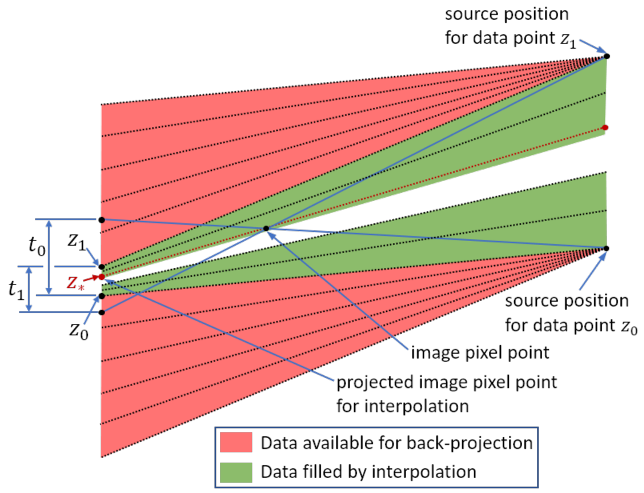

Fig. 3: Illustration of the vertical cross section of the areas illuminated by two vertically-shifted source positions. Image pixels lying on the same dotted line share the same z_* value. Red region shows where the projection data is originally available, and green region shows where the synthetic projection data is filled by interpolation.

For illustration purposes, let us assume that the object is stationary, and the source-detector gantry is shifting vertically. Since we interpolate two (filtered) cone beam projections with the vertically-shifted source-detector positions, the horizontal coordinate of the interpolated data is still the same in both cases. Only the vertical coordinate of one illuminated region is shifted relative to the other. The illuminated regions for the two projections do not overlap, and there is a gap between the two illuminated regions where the projection data are not available. Fig. 3 shows the schematic vertical cross section of the two illuminated regions and the gap between them.

Two data points (z_0 and z_1 in Fig. 3) to be used for interpolation do not share the same mapping onto the detector vertical coordinate, as the mapping depends on the vertical source positions. Thus, the interpolated projection data does not belong to any of those two mapping systems. To solve this issue, we define a set of virtual source positions between the two actual source locations, that enables the projected vertical coordinate of the data point to always be between the top of the bottom projection data region and the bottom of the top projection data region. Additionally, to avoid estimating values too far from the available data, we apply interpolation only to image pixels if their projected vertical coordinate is within a threshold distance of z_e from either the top source position or the bottom source position (see the green regions in Fig. 3). Consequently, the following value is used in the interpolation algorithm to identify the location of the interpolated data point:

$$z_* = \frac{z_0 t_1^{n_\mathrm{I}} + z_1 t_0^{n_\mathrm{I}}}{t_0^{n_\mathrm{I}} + t_1^{n_\mathrm{I}}}, \quad z_0 < z_* \leq z_0 + z_e \text{ or } z_1 - z_e \leq z_* < z_1. \tag{7}$$

where t_0 is the vertical distance between the reference data point z_0 and the shadow of the image point with the corresponding source position, t_1 is the equivalent of t_0 with the reference data point being z_1.

Boundary detector pixels are more vulnerable to high amplitude noise as they have fewer neighboring pixels that can be used for denoising. Nearest neighbor interpolation makes the image more crisp, but it can create discontinuity and amplify noise. Linear interpolation attenuates noise, but it reduces spatial resolution. The factor $n_\mathrm{I} > 0$ provides the flexibility to transform the interpolator from linear to nearest neighbor, i.e., linear interpolation if $n_\mathrm{I} = 1$, and nearest neighbor if $n_\mathrm{I} \gg 1$.

V. Numerical Experiments

We simulate noise-free sinogram data for a 3D phantom consisting of water, aluminum, and titanium ellipsoids (see Fig. 4), with poly-energetic sources fired in a periodic quasi-random sequence.

Fig. 5 shows the estimated coefficients c_p and c_s without any streak artifact removal applied. Note that the c_s image has significantly fewer streaks than the c_p image. Fig. 6 shows the corresponding coefficients after data-filling and MBL filter are applied. Without artifact correction, the intensity of streaks in the c_p image is much greater than the value of c_p for water, thus making the estimation of ρ and Z_eff almost impossible. The proposed streak removal workflow enables one to estimate ρ and Z_eff based on (2). Figs. 7 and 8 show the profiles of ρ and Z_eff in four different locations marked by colored lines in Fig. 4. While the estimated ρ deviates from the ground truth, the estimated Z_eff matches well with the ground truth. The error in the density estimation is mostly caused by two factors: (1) cone-beam error of the FDK-type reconstruction, (2) approximation error of $Z/A = 0.5$. Fortunately, estimation of the effective atomic number is less vulnerable to those two errors because they affect both the c_p and c_s equally. Dividing c_p by c_s compensates the error. Also, the error in density due to the Z/A approximation is systematic and should not affect material identification since this can be calibrated.

VI. Conclusions

We develop a workflow for robust MECT image reconstruction for a stationary gantry scanner. The presented numerical experiments demonstrate that the proposed algorithms allow one to efficiently reduce streak artifacts while preserving the accuracy of ME-SGCT reconstruction.

References

[1] A. Katsevich, S. Yoon, M. Frenkel, E. Morton, and W. Thompson, "Reduction of irregular view-sampling artifacts in a stationary gantry ct scanner," in 15th International Meeting on Fully Three-Dimensional Image Reconstruction in Radiology and Nuclear Medicine, vol. 11072. International Society for Optics and Photonics, 2019, p. 110720G.

[2] R. E. Alvarez and A. Macovski, "Energy-selective reconstructions in X-ray computerized tomography." Physics in medicine and biology, vol. 21, no. 5, pp. 733–744, 1976.

[3] M. Paziresh, A. M. Kingston, S. J. Latham, W. K. Fullagar, and G. M. Myers, "Tomography of atomic number and density of materials using dual-energy imaging and the Alvarez and Macovski attenuation model," Journal of Applied Physics, vol. 119, no. 21, 2016.

[4] M. Salehjahromi, Y. Zhang, and H. Yu, "Iterative spectral CT reconstruction based on low rank and average-image-incorporated BM3D," Physics in Medicine and Biology, vol. 63, 2018, article id 155021.

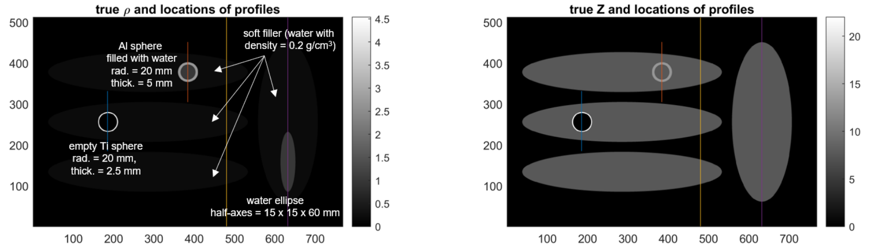

Fig. 4: Ground truth phantom data, density ρ (left) and effective atomic number Z_{eff} (right). Lines indicate the locations of profiles shown in Figs. 7 and 8.

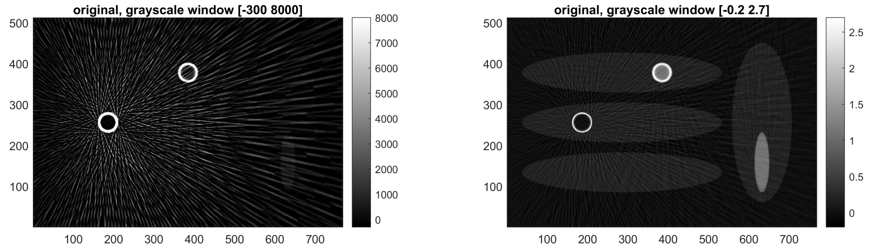

Fig. 5: Estimated c_{p} (left) and c_{s} (right), without data-filling or MBL filtering.

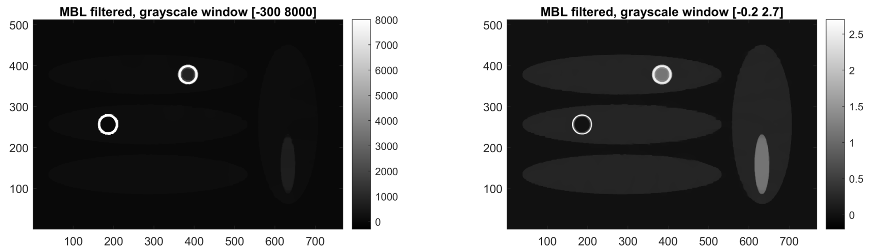

Fig. 6: Estimated c_{p} (left) and c_{s} (right), after data-filling and MBL filtering.

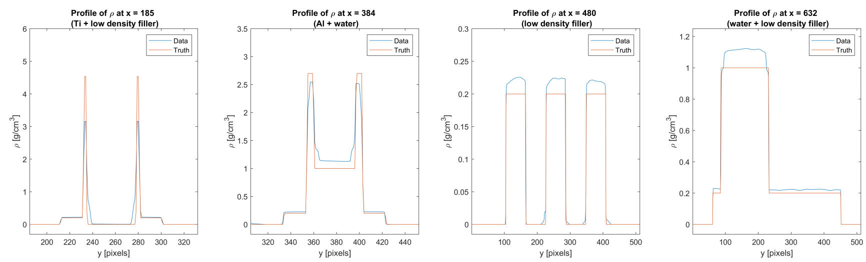

Fig. 7: Profiles of estimated density after data-filling and MBL filtering. Locations of the sampled profiles are shown in Fig. 4.

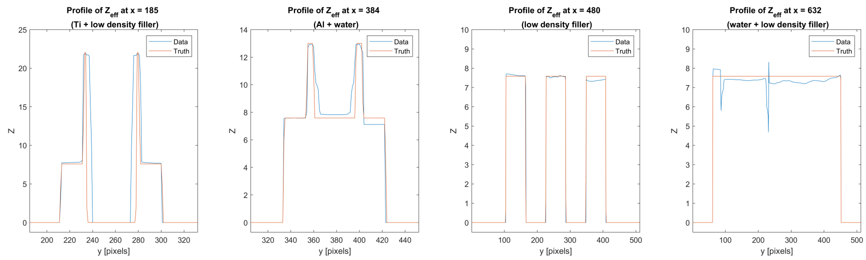

Fig. 8: Profiles of estimated effective atomic number after data-filling and MBL filtering. Locations of the sampled profiles are shown in Fig. 4.